Bulletin of the Seismological Society of America, Vol. 96, No. 2, pp. 365–376, April 2006, doi: 10.1785/0120050130

Uncertainty of Earthquake Losses due to Model Uncertainty of Input Ground Motions in the Los Angeles Area

by Tianqing Cao and Mark D. Petersen

Abstract In a recent study we used the Monte Carlo simulation method to evaluate the ground-motion uncertainty of the 2002 update of the California probabilistic seismic hazard model. The resulting ground-motion distribution is used in this article to evaluate the contribution of the hazard model to the uncertainty in earthquake loss ratio, the ratio of the expected loss to the total value of a structure. We use the Hazards U.S. (HAZUS) methodology for loss estimation because it is a widely used and publicly available risk model and intended for regional studies by public agencies and for use by governmental decision makers. We found that the loss ratio uncertainty depends not only on the ground-motion uncertainty but also on the mean ground-motion level. The ground-motion uncertainty, as measured by the coefficient of variation (COV), is amplified when converting to the loss ratio uncertainty because loss increases concavely with ground motion. By comparing the ground-motion uncertainty with the corresponding loss ratio uncertainty for the structural damage of light wood-frame buildings in Los Angeles area, we show that the COV of loss ratio is almost twice the COV of ground motion with a return period of 475 years around the San Andreas fault and other major faults in the area. The loss ratio for the 2475-year ground-motion maps is about a factor of three higher than for the 475-year maps. However, the uncertainties in ground motion and loss ratio for the longer return periods are lower than for the shorter return periods because the uncertainty parameters in the hazard logic tree are independent of the return period, but the mean ground motion increases with return period.

Introduction

In a recent study, Cao *et al.* (2005) used the Monte Carlo simulation method to calculate ground-motion distributions and ground-motion uncertainty maps for the 2002 California probabilistic seismic hazard model. In this simulation study, the California seismic hazard logic tree for the 2002 hazard maps is sampled to account for the seismic hazard model (epistemic) uncertainty. The simulated ground-motion uncertainty varies with the number of simulations used and converges with increasing number of simulations. We found that about 100 simulations of ground-motion hazard achieved a variation less than 5%. In the study of Cao *et al.* (2005), 150 simulations were used. As a result, we produced 150 ground-motion maps for a particular probability of exceedance in certain years, which formed a ground-motion distribution at a 0.05-degree grid across certain areas in California. The ground-motion uncertainty, such as the coefficient of variation (standard deviation divided by mean, COV), was derived from the ground-motion distribution, for example, at 10% probability of exceedance in 50 years (a return period of 475 years).

One application of the ground-motion distributions and uncertainty maps is to estimate the hazard-model contribution to the uncertainty of the scenario expected loss ratio, in which the mean loss is associated with the ground motion of a particular return period. We use the public loss estimation methodology, HAZUS, which stands for Hazards U.S. (National Institute of Building Sciences [NIBS], 1997 and 2002), to estimate the loss for each of these ground-motion maps and then obtain the loss ratio uncertainty. Direct use of the HAZUS software for our calculation is not practical for the following two reasons. First, it is not efficient to run HAZUS 150 times for thousands of sites in the Los Angeles area because of the computing time needed. Second, to analyze the results, we have to perform sensitivity tests on input ground motions and model parameters; the software package HAZUS does not provide such a utility. Therefore, we wrote our own program for the calculations but followed the HAZUS design step by step in our program. Many numerical tests were performed and the test results from our program were compared with HAZUS. The comparison showed that most of the test results from our program were nearly identical with the HAZUS results and the

rest were within a few percent of the HAZUS results. These tests covered a wide range of input ground motions of spectral acceleration (SA) at 0.3 sec from 0.2 to 1.4*g*. In our program, we included some necessary formulas that were not documented in the technical manual of HAZUS (NIBS, 1997 and 2002; referenced as the Manual in the following) or other relevant publications. Therefore, a complete formulation used in the program is presented in the Appendix. To clearly distinguish the origins of formulas, we will indicate the page number if a referred formula is from the HAZUS manual; otherwise they are from our interpretation of the HAZUS model.

The loss ratio uncertainty is mostly from the uncertainties of input ground motion, site condition, and the conversion from ground motion to loss or the vulnerability relation. In this article, we study the loss ratio uncertainty due to ground-motion uncertainty only. The site-condition correction to ground motion is being included in the Pacific Earthquake Engineering Research's Next Generation Attenuation (NGA) relations (http://peer.berkeley.edu/NGA_program/) using the average shear velocity in the upper 30 m (V_{S30}). It will be more appropriate to study the loss ratio uncertainty due to the site-condition correction when these new attenuation relations are released. The uncertainty data on the vulnerability relations are mostly proprietary and not available for this study. Some of the uncertainties, such as the conditional variability of building performance (performance uncertainty) and its interaction with the attenuation uncertainty are also not considered here.

Cao *et al.* (2005) find that because the uncertainty parameters assigned in the logic tree of the 2002 California hazard model are independent of the return period, the ground-motion uncertainties for very long return periods are underestimated. Therefore, we choose to calculate the loss ratios due to given ground motions of a relatively short return period of 475 years and a long return period of 2475 years (10% and 2% probability of exceedance in 50 years, respectively) for comparison. The loss ratio uncertainties for other return periods can be calculated the same way with ground-motion distributions for other return periods. In this study, the ground motions from probabilistic seismic hazard analysis are applied like the ground motions from a scenario event so that the loss ratio from this study is the scenario expected loss ratio and not the expected annualized loss ratio, which is evaluated from the ground motions of multiple return periods in HAZUS.

Input Ground Motions

The logic tree for the 2002 California hazard model (Frankel *et al.*, 2002) contains five nodes, as discussed in Cao *et al.* (2005). They are associated with the selection and weighting of attenuation relations, fault area-magnitude relations, characteristic versus Gutenberg–Richter recurrence modeling, epistemic magnitude uncertainty, and fault slip rate uncertainty. Along each of these nodes there are two or more branches that define alternative hazard models. The Monte Carlo simulation samples the logic tree and selects different combinations of these branches or different complete viable hazard models. Each simulation produces a ground-motion map for a given probability of exceedance in certain years by contouring the ground-motion values at grid sites. In the study of Cao *et al.* (2005), 150 ground-motion maps are computed for the Los Angeles area. These maps together provide a distribution of ground motion for each site on the map. These ground-motion maps are the input to our loss ratio uncertainty estimation.

Figure 1 shows the fault distribution in the Los Angeles area. Class A faults are active faults with better known rupture histories and class B faults are active faults with unknown or uncertain rupture histories. Figure 2 shows the mean SA at 0.3 sec (SA_{03}) at a 10% probability of exceedance in 50 years from the 150 simulations. The SA map shows that the hazard distribution is controlled by the fault distribution and the highest hazards are located along the San Andreas fault. However, the highest uncertainties of SA are not along the San Andreas fault but offshore around the Channel Islands Thrust fault and the Anacapa-Dume fault with poorly defined slip rates. Figure 3 is a contour map showing the COV of SA_{03}. The COV values for SA_{03} range from 0.10 to 0.20 at locations near the major onshore faults

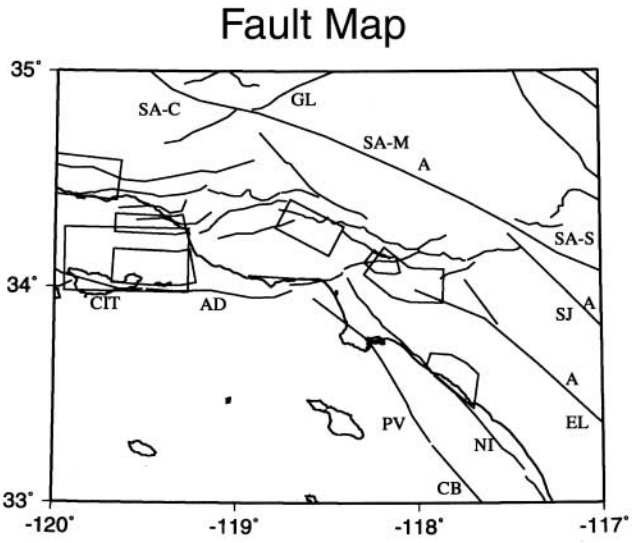

Figure 1. The fault map for the Los Angeles area. The class A faults are labeled with "A," which are active faults with rupture histories; the others are class B faults, which are active with unknown rupture histories. Blind thrust faults are indicated by polygons, which are their surface projections. The abbreviations are "SA-M" for the Mojave segment of the San Andreas fault, "SA-C" for the Carrizo segment, "SA-S" for the San Bernardino segment, "GL" for the Garlock fault, "SJ" for the San Jacinto fault, "EL" for the Elsinore fault, "NI" for the Newport-Inglewood fault, "CB" for the Coronado Bank fault, "PV" for the Palos Verdes fault, "AD" for the Anacapa-Dume fault, and "CIT" for the Channel Islands Thrust fault.

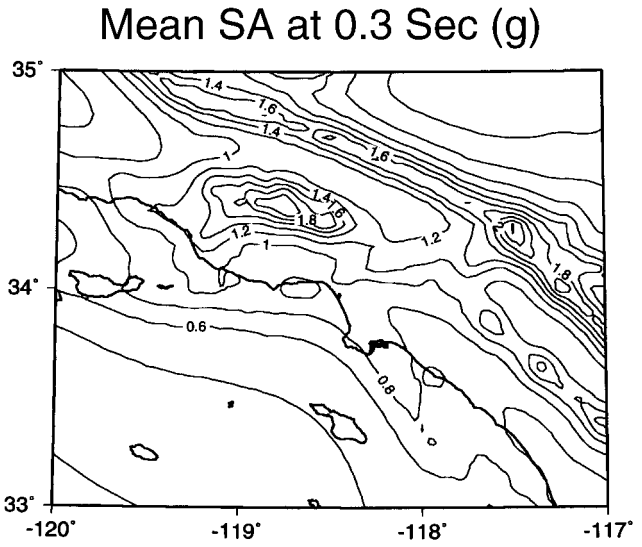

Figure 2. Contour map for the mean SA at 0.3 sec with a return period of 475 years in the Los Angeles area. The mean value is from averaging the 150 Monte Carlo simulations.

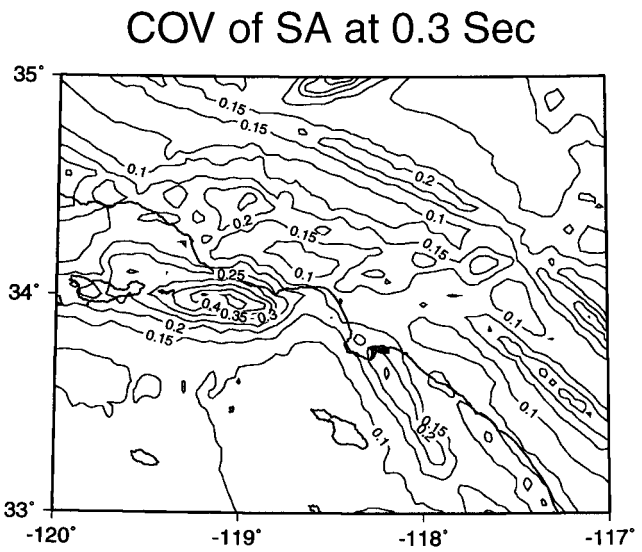

Figure 3. Contour map for the COV of 0.3 sec SA with a return period of 475 years in the Los Angeles area.

and decrease slightly away from the faults. Near the offshore faults mentioned previously, the COV values are higher and in the range of 0.2 to 0.4.

In the next section we briefly summarize the HAZUS approach for loss estimation that is followed in this study. In the Appendix we thoroughly document the formulas used in our program for calculating the loss ratio. These formulas are from the HAZUS Manual or according to our understanding of the HAZUS approach. The test results from our program and from HAZUS are also compared in the next section.

Loss Estimation Method

The HAZUS methodology is a publicly available loss estimation computation and used in many regional seismic loss assessments in United States. This method updates the previous public loss model for loss estimation that is based on damage probability matrix (Whitman *et al.*, 1973; Applied Technology Council, 1985) and described in Cao *et al.* (1999). The HAZUS method uses response spectrum, building capacity curve, and push-over analysis to determine the spectral displacement (SD) and then uses the SD to determine the probabilities of damage for different damage states (Manual, 1997 and 2002). The response spectrum is constructed using SA at 0.3 and 1.0 sec. In HAZUS, the building damage states are classified into five discrete levels: none, slight, moderate, extensive, and complete. These damage states are directly related to the percentage of building replacement cost. The loss ratio to a building structure, for example, is the summation of damage probability (the probability of a particular damage state) multiplied by the structure damage rate (the economic loss of structure damage as a percentage of the replacement cost for a particular damage state) for all damage states.

With those formulas in the Appendix we calculated the loss ratio for given ground motions. In Table 1 the damage probabilities for the five damage states calculated using HAZUS-99 and our own program for the W1 (light wood frame) type of buildings are compared for six test cases. The input ground motions for these tests are arbitrarily selected from the 2002 California hazard maps (Frankel *et al.*, 2002) to cover a wide range of levels. Other parameters, which are defined in the formulas (Appendix) using these parameters, are as follows: the parameters to define a capacity curve for the W1-type buildings, which are the pairs of SA and displacement coordinates for the yield and ultimate points, are $D_y = 0.48$ (inches), $A_y = 0.40$ (g), $D_u = 11.51$ (inches), and $A_u = 1.20$ (g) for the high-code design level (Manual, table 5.7a on page 5-31). The parameter κ, which is the degradation factor and related to the shaking duration, is 0.5 for long ground-shaking duration (Manual, table 5.18 on page 5-65). The elastic damping coefficient, β_e, is 15%. Structural fragility curve parameters used in formulas (A15) and (A16) (Appendix) are median peak-response displacement m_i (0.5, 1.51, 5.04, and 12.60 inches) and its variability β_i (0.8, 0.81, 0.85, and 0.97 inches) for i from 1 to 4 for the high-code seismic-design level (Manual, table 5.9a on page 5-41).

Table 1 shows that in most cases our program yielded results nearly identical with HAZUS, and in a few cases the differences are within a few percent. Our numerical testing showed that we can always find a displacement to get five damage probabilities that match the HAZUS results exactly by using formulas (A16) and (A17) in the Appendix. We conclude that the small differences in Table 1 must be from the different solutions of peak-response displacements, which are solved in an iterative process by using formula

Table 1
Comparison of the Damage Probability

Input Ground Motion (g)			Damage Probability (HAZUS/This Study)				
SA_{03}	SA_{10}	PGA	None	Slight	Moderate	Extensive	Complete
0.219	0.115	0.101	0.91/0.91	0.09/0.09	0.00/0.00	0.00/0.00	0.00/0.00
0.373	0.169	0.175	0.75/0.75	0.23/0.23	0.02/0.02	0.00/0.00	0.00/0.00
0.645	0.246	0.311	0.49/0.50	0.42/0.41	0.09/0.08	0.00/0.00	0.00/0.00
0.782	0.285	0.380	0.38/0.40	0.48/0.47	0.14/0.13	0.01/0.01	0.00/0.00
1.155	0.535	0.563	0.17/0.19	0.49/0.50	0.30/0.27	0.03/0.02	0.01/0.01
1.382	0.669	0.669	0.11/0.11	0.45/0.45	0.38/0.38	0.05/0.05	0.01/0.01

(A10) in the Appendix. Formula (A10) defines the area of a parallelogram (see Fig. A4 in the Appendix), which is the area enclosed by the hysteresis loop at peak-response displacement D and acceleration A (Manual, page 5-65). This area of the hysteresis loop defined by formula (A10) may be slightly different from HAZUS.

Loss Ratio as a Function of Ground Motion and Loss Ratio Uncertainty Maps

To study the loss ratio of the structural damage for type W1 buildings in the Los Angeles area, it is helpful to investigate the general relation between ground motion and loss ratio first. This relation is usually called the vulnerability function. The ground-motion data in Table 1 reveal that SA at 1.0 sec is about half of the value at 0.3 sec. If we assume this ratio then we can calculate the loss ratio as a function of SA at 0.3 sec only. We will show that this assumption only affects the calculated vulnerability function at very high ground motions and has very little impact on our discussion of the Los Angeles area. In this area the ground motions are at moderate levels for the moderate 475-year return period and the National Earthquake Hazards Reduction Program (NEHRP) B-C site condition. For other conditions, the spectral shape might be much different.

Figure 4 is the calculated relation (vulnerability function) between structural loss ratio (not total loss ratio) and ground motion SA at 0.3 sec. The structural damage rates R_i used in the calculation, which are the direct economic losses as a percentage of the replacement cost (see formula A18 in the Appendix), are 2%, 10%, 50%, and 100% for the four damage states from slight to complete. In some vulnerability relations, the ground motion also can be PGA or ground-shaking intensity (Cao *et al.*, 1999). Figure 4 shows that the structural loss ratio increases concavely with SA until SA reaches about 2.5g where the vulnerability curve has a sudden slope change. This sudden slope change happens at the transition from the constant SA to the constant spectral velocity (SV) on a demand spectrum (see Fig. A3 in the Appendix). This transition means that the vulnerability function before and after the slope change is determined by SA at 0.3 and 1.0 sec, respectively. Therefore, the preceding assumption that SA at 1 sec is about half of the value at 0.3 sec only affects part of the vulnerability curve slightly (Fig. 4) after the transition point, which happens at SA greater than 2.5g. This ground-motion level is rarely reached in California on a map of 475-year return period (10% probability of exceedance in 50 years). Hence, the preceding assumption does not affect the validity of Figure 4. Figure 4 is the vulnerability function of HAZUS for light wood-frame buildings (W1) and it fully defines the structural loss ratio for given ground motions and therefore the loss ratio uncertainty from the percentage uncertainty of ground motion. The shape of this vulnerability curve is very similar to the ATC-13 vulnerability curve (Cao *et al.*, 1999). Because we used the W1 high-code design-damage relationship of HAZUS, which is representative of the recent design, this curve underestimates the damage to old constructions. A detailed study of old construction in the Los Angeles area was presented by Wesson *et al.* (2004). Note also that the uncertainty of the vulnerability curve contributes significantly to the loss ratio COV, which is not included in this study.

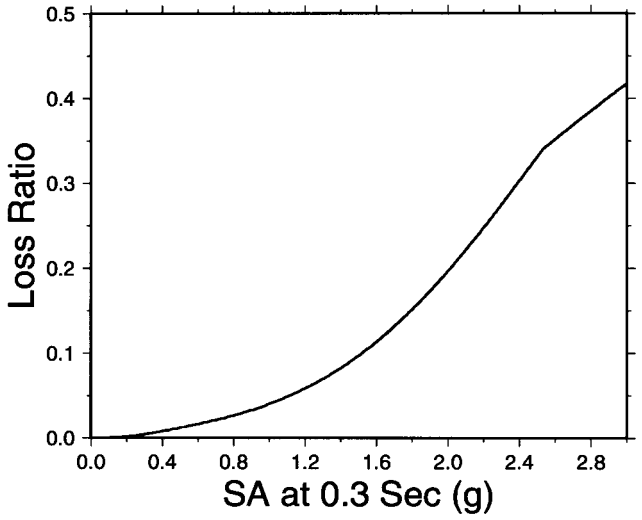

Figure 4. A vulnerability curve showing loss ratio as a function of 0.3 sec SA. The curve increases concavely with ground motion up to 2.5g and then has a sudden slope decrease. The sudden slope decrease happens at the transition point of the demand spectrum, where it changes from a region of constant SA to a region of constant SV.

From the previous relation between loss ratio and ground motion, it becomes evident that loss ratio uncertainty depends not only on the uncertainty of ground motion but also on the mean ground-motion level. We should investigate how the loss ratio increases with increase of ground motion from different mean ground-motion levels or the percentage increase of loss ratio versus the percentage increase of ground motion from different mean levels (Fig. 5). First we see that the loss ratio increases almost linearly with the percentage increase of ground motion for all mean ground-motion levels. For mean SA (0.3 sec) value at 1*g*, the rate of increase of loss ratio is about 2 (the slope of curve A), which means that if SA increases 10% from 1*g* (mean) the loss ratio increases about 20%. So the COV of ground-motion uncertainty is amplified when converting to COV of loss ratio uncertainty. This amplification is due to the concave increase of loss ratio with ground-motion increase (Fig. 4). Second, we see that if the mean SA value increases, for example, from curve A (1*g*) to curve B (1.2*g*) in Figure 5, the curve slope (the increase rate of loss ratio) increases. The rate of increase reaches a plateau or saturates at mean ground-motion values at about 1.4 to 1.6*g* (curves C and D). The amplification from ground-motion COV to loss ratio COV increases with mean ground motion and saturates at certain mean ground-motion levels and then decreases slightly (curve E). The saturation of amplification is the result of the slope change of the vulnerability curve in Figure 4 that the loss ratio increases concavely with ground motion and then has a slope decrease starting at about 2.5*g*. The sudden slope change of curve E (Fig. 5) at about 40% increase of ground motion is due to the transition from constant SA to the constant SV (see Fig. A1), which happens when SA reaches 2.5*g* (1.8 × 140% = 2.52) as shown in Figure 4. The other curves with lower mean ground-motion values in Figure 5 never reach this high ground-motion level even with ground-motion increases up to 50% and, therefore, do not show a sudden slope change.

Figure 6 shows the mean loss ratio in the Los Angeles area, which is calculated using formula (A18) in the Appendix. We see that the loss ratio follows the mean SA at 0.3 sec (Fig. 2) closely. Figure 7 is the COV contour map for the loss ratio, which is obtained in two steps: (1) calculating 150 loss ratio maps from 150 ground-motion maps and (2) calculating the loss ratio COV map from the standard deviation and mean of loss ratio. Because of the amplification from ground-motion uncertainty to loss ratio uncertainty, the COV values of loss ratio (Fig. 7) are higher than the COV values of ground motion (Fig. 3). Around the San Andreas fault and other major faults, where the SA (0.3 sec) values range from 1.6 to 2.0*g* (Fig. 2), the COV value for loss ratio (Fig. 7) is about twice the COV value for SA (Fig. 3). In the areas further away from the San Andreas fault and other major faults, where the mean SA decreases to about 1*g* or lower and the COV of SA decreases to 0.1 to 0.15 (Figs. 2 and 3), the amplification factor from COV of ground motion to COV of loss ratio is about 1.5, which is lower than around the major faults due to the lower mean ground motions (Fig. 5). In the area south of the intersection between the San Andreas fault and the Garlock fault, where the COV of ground-motion ranges from 0.2 to 0.25 (Fig. 3), which is similar to the COV around the San Andreas fault, the COV of loss ratio (Fig. 7) in this area is about 0.25 and is much lower than the value ranging from 0.35 to 0.45 around the San Andreas fault. This

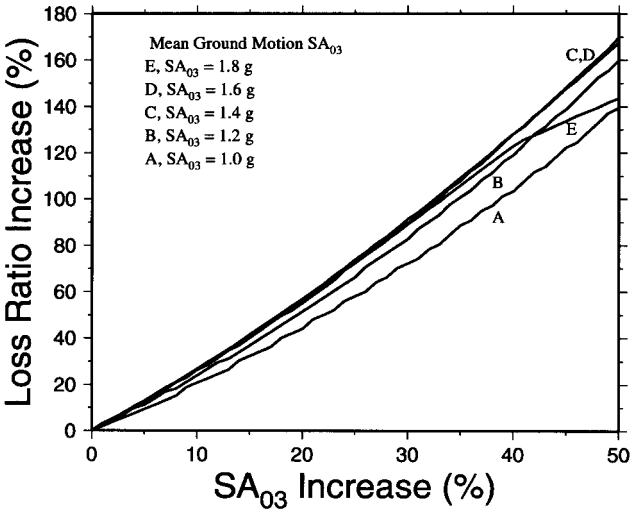

Figure 5. Loss ratio increase as a function of ground-motion percentage increase. This relationship depends nonlinearly on the mean ground-motion level. The percentage increase of ground motion is amplified when converting to the percentage increase of loss ratio. The amplification factor increases with mean ground-motion value and saturates at about 1.4 to 1.6*g*, which is related to the slope change of the vulnerability curve in Figure 4.

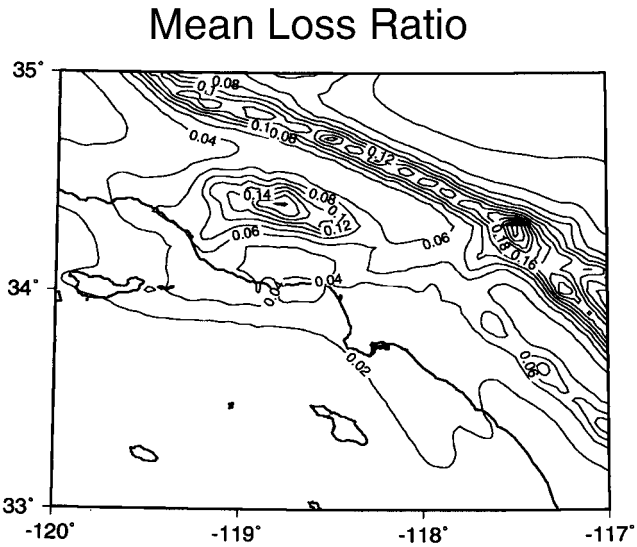

Figure 6. Contour map for the mean loss ratio from ground motions with a return period of 475 years. It follows the mean ground-motion map (Fig. 2) closely.

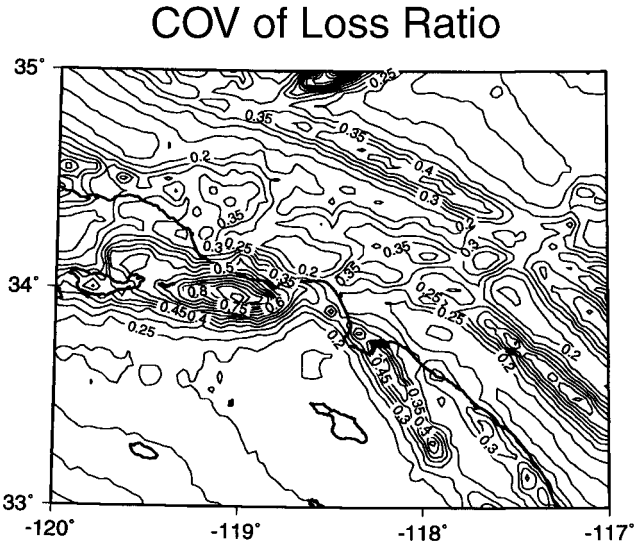

Figure 7. Contour map for the COV of the loss ratios, which are from the ground motions with a return period of 475 years. To compare with the ground-motion COV map (Fig. 3), we see the COV of loss ratio is amplified but not uniformly. The amplification depends on the ground-motion values nonlinearly as shown in Figure 5.

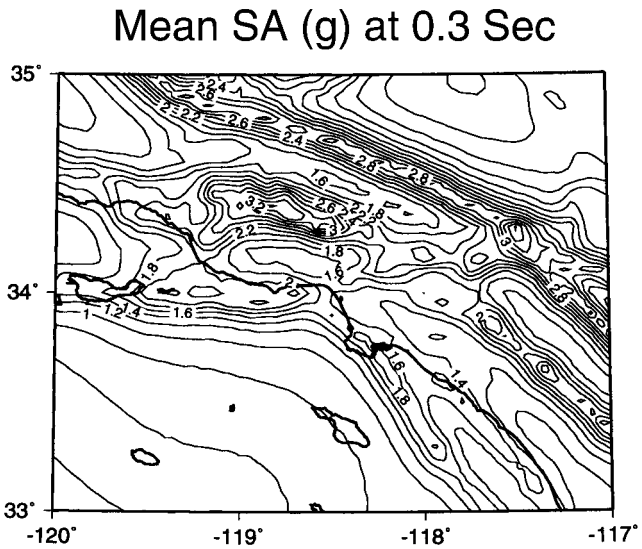

Figure 8. Contour map of the mean 0.3 sec SA with a return period of 2475 years in the Los Angeles area. The mean value is from averaging the 150 Monte Carlo simulations.

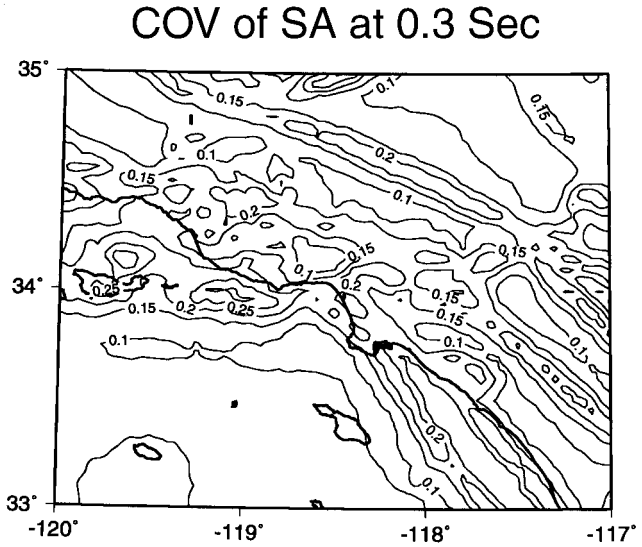

Figure 9. Contour map for the COV of the 0.3 sec SA with a return period of 2475 years in the Los Angeles area.

difference between loss uncertainties for the two areas with similar COV of ground motion is also due to the mean ground-motion difference (Fig. 2). In addition to the mean ground-motion dependence, the amplification depends also on building types, although this study is only for W1-type buildings.

From the ground motions of any return period we can produce the mean ground motion, COV of ground motion, mean loss ratio, and COV of loss ratio maps corresponding to the maps in Figures 2, 3, 6, and 7 for the return period of 475 years. For the return period of 2475 years (2% probability of exceedance in 50 years), the mean ground motions (Fig. 8) are much higher than for the return period of 475 years (Fig. 2). But the COV values of ground motion for the longer return period (Fig. 9) are lower than for the shorter return period (Fig. 3). This surprising result is due to the limitations of our knowledge on the uncertainty parameters in the logic tree for probabilistic hazard uncertainty analysis (Cao *et al.*, 2005). Currently these parameters, for example, the epistemic magnitude uncertainty, are independent of the return period. When the return period increases, the ground motion increases but not its uncertainty and causes the COV to decrease. The mean loss ratios for the 2475-year return period (Fig. 10), which are determined by the ground-motion levels, are much higher than for the 475-year return period (Fig. 6). Along the major faults in the area, such as the San Andres fault, the mean loss ratio for the 2475-year return period is about three times of the mean loss ratio for the 475-year return period. The COV values of loss ratio for the 2475-year return period (Fig. 11) are lower than the COV values for the 475-year return period (Fig. 7). This is due to the decrease of ground motion COV with increasing return period (Cao *et al.*, 2005). Because this decrease is due to the limitations of our current knowledge on uncertainty parameters and will affect the annualized loss uncertainty estimation, in which ground motions of multiple return periods are used, we limit the loss uncertainty estimation to the scenario expected loss ratio only in this study.

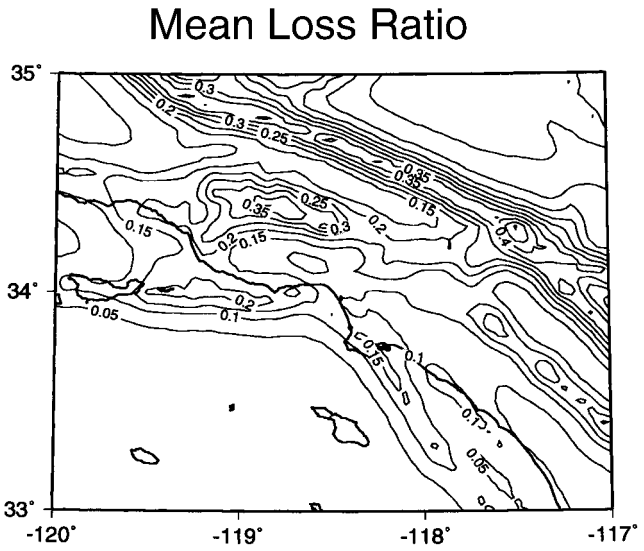

Figure 10. Contour map for the mean loss ratio from ground motions with a return period of 2475 years. It follows the mean ground-motion map (Fig. 8) closely.

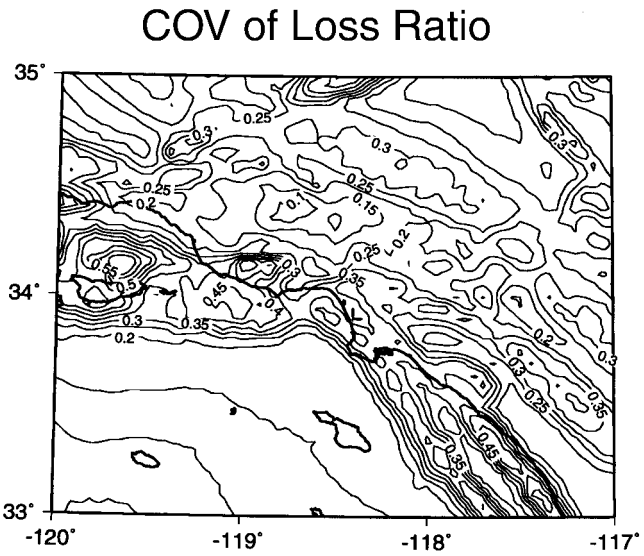

Figure 11. Contour map for the COV of the loss ratios, which are from the ground motions with a return period of 2475 years. To compare with the ground-motion COV map (Fig. 9), we see the COV of loss ratio is amplified but not uniformly. The amplification depends on the ground-motion values nonlinearly as shown in Figure 5.

Summary and Discussions

In this study we have used the ground-motion uncertainty maps from Monte Carlo simulations to obtain the loss ratio uncertainty map for the structural damage of the light wood-frame buildings in the Los Angeles area. We followed the widely used risk model HAZUS for loss estimation. We calculated the vulnerability function for the structural damage of the light wood-frame buildings and the loss ratio uncertainty from the uncertainty of ground motion in the Los Angeles area. We found that the uncertainty of ground motion, which is measured by the COV, is amplified when converting to COV of loss ratio. The amplification is nonlinear and depends on the mean ground-motion level. It increases with mean ground up to about 1.4 to 1.6g, then saturates and decreases at higher levels. In the Los Angeles area, the mean loss ratio tracks the mean SA at 0.3 sec. Note that the part of the damage function for SA greater than 2.5g is an extrapolation because such level of ground motions has not yet been recorded in W1-type structures.

This study only estimated the loss ratio uncertainty for the structural damage of the light wood-frame buildings due to the input ground-motion uncertainty; many other components of the uncertainty were not assessed. The overall uncertainty of loss estimation should include the model uncertainty of the loss estimation method and the uncertainties of all the model parameters, such as the uncertainty of building inventory. That is beyond the scope of this study and requires input from engineers. This article is also limited to quantifying the uncertainty of loss ratio only for the ground motions of one risk level, which is treated as ground motions from a scenario event. We did not evaluate the uncertainty for the annualized loss, which uses ground motions from different return periods and will add more uncertainties to the overall uncertainty.

In this study we considered only a single-site condition (NEHRP B-C). The ground-motion uncertainty due to the site-condition correction is not counted. We are conducting a special study on such uncertainty using the newly developed NGA attenuation relations, in which V_{S30} is used to predict the soil amplification of ground motion.

Acknowledgments

We are grateful to Chris Wills, Mike Reichle, and Dave Branum for many helpful discussions. We thank Ivan Wong, Kenneth Campbell, and an anonymous reviewer for their critical reviews. We are also grateful to E. V. Leyendecker for checking the formulas and calculations.

References

Applied Technology Council (1985). *Earthquake Damage Evaluation Data for California* (ATC-13), Applied Technology Council, Redwood City, California.

Cao, T., M. D. Petersen, C. H. Cramer, T. R. Toppozada, M. S. Reichle, and J. F. Davis (1999). The calculation of expected loss using probabilistic seismic hazard, *Bull. Seism. Soc. Am.* **89,** 867–876.

Cao, T., M. D. Petersen, and A. D. Frankel (2005). Model uncertainties of the 2002 update of California seismic hazard maps, *Bull. Seism. Soc. Am.* **95,** 2040–2057.

Chopra, A. K. (1995). *Dynamics of Structures*, Prentice Hall, Engelwood Cliffs, New Jersey.

Federal Emergency Management Agency (FEMA) (1997). NEHRP Commentary on the Guidelines for the Seismic Rehabilitation of Buildings, FEMA 274, Washington, D.C.

Frankel, A. D., M. D. Petersen, C. S. Mueller, K. M. Haller, R. L. Wheeler, E. V. Leyendecker, R. L. Wesson, S. C. Harmsen, C. H. Cramer,

D. M. Perkins, and K. S. Rukstales (2002). Documentation for the 2002 update of the national seismic hazard maps, *U.S. Geol. Surv. Open-File Rept. 02-420*.

Leyendecker, E. V., R. J. Hunt, A. D. Frankel, and K. S. Rukstales (2000). Development of maximum considered earthquake ground motion maps, *Earthquake Spectra* **16,** no. 1, 21–40.

National Institute of Building Sciences (NIBS) (1997). Earthquake loss estimation methodology, HAZUS97 (SR1): technical manual, Report prepared for the Federal Emergency Management Agency, NIBS, Washington, D.C.

National Institute of Building Sciences (NIBS) (2002). Earthquake loss estimation methodology, HAZUS02 (SR2): technical manual, Report prepared for the Federal Emergency Management Agency, NIBS, Washington, D.C.

Newmark, N. M., and W. J. Hall (1982). *Earthquake Spectra and Design*, Earthquake Engineering Research Institute (EERI) Monograph, EERI, Oakland, California.

Wesson, R. L., D. M. Perkins, E. V. Leyendecker, R. J. Roth, and M. D. Petersen (2004). Losses to single-family housing from ground motions in the 1994 Northridge, California, earthquake, *Earthquake Spectra* **20,** no. 3, 1021–1045.

Whitman, R. V., J. W. Reed, and S. T. Hong (1973). Earthquake damage probability matrices, in *Proc. of the 5th World Conference on Earthquake Engineering*.

Appendix

Formulation of Loss Estimation

The HAZUS method uses the response spectrum, building capacity curve, and push-over analysis to determine SD and then uses SD to calculate the probabilities of damage for different damage states (Manual, 1997 and 2002). The loss ratio to a building structure, for example, is the summation of damage probabilities multiplied by the structure damage rate for each damage state. In this Appendix we present a complete formulation for the estimation of loss ratio.

Elastic Response Spectrum of 5% Critical Damping

The response spectrum of 5% critical damping is defined by the given ground motions of peak ground acceleration (PGA) and SA at 0.3 (SA_{03}) and 1.0 (SA_{10}) sec, which characterize the ground-shaking demand (Manual, page 4-3). These spectra have the same "standard" format (Fig. A1a, also Manual, page 4-8) that consists of three parts: (1) a region of constant SA at short periods (acceleration domain), (2) a region of constant SV at long periods (velocity domain), and (3) a region of constant SD at very long periods (see Fig. A1 and Manual, page 4-8). This response spectrum is a modified version at short periods that constant SA_{03} extends to period $T = 0$ and PGA is not used (Fig. A1).

A slightly different definition for the early part of the response spectrum can be found in Leyendecker *et al.* (2000), where the constant is not the SA value at 0.3 but at 0.2 (SA_{02}) sec. The connecting point between constant SA and constant SV is at a period T_{av}. Because the constant SV part of the curve is proportional to $1/T$ and anchored to SA_{10}, we have $SA = SA_{10}/T$. For the connecting point with constant SA, we have $SA_{03} = SA_{10}/T_{av}$ or $T_{av} = SA_{10}/SA_{03}$. The connecting point between constant SV region and constant SD region is at period T_{vd}, which is the reciprocal of the corner frequency f_c. The corner frequency is determined by the earthquake's moment magnitude M (Manual, page 4-8), so we have $T_{vd} = 1/f_c = 10^{(M-5)/2}$. Now we have the expressions for the three regions of a response spectrum as following:

$$SA = SA_{03}, \quad 0 \le T \le T_{av}, \tag{A1a}$$

$$SA = SA_{10}/T, \quad T_{av} \le T \le T_{vd}, \tag{A1b}$$

$$SA = SA_{10}T_{vd}/T^2, \quad T \ge T_{vd}. \tag{A1c}$$

Because the response spectrum is going to be used with the building capacity curve, which is usually expressed as a relation between SA and SD, it is convenient to convert these expressions of SA as functions of period T to the expressions of SA as functions of SD. These SA and SV are all pseudo variables, so we have the following relations:

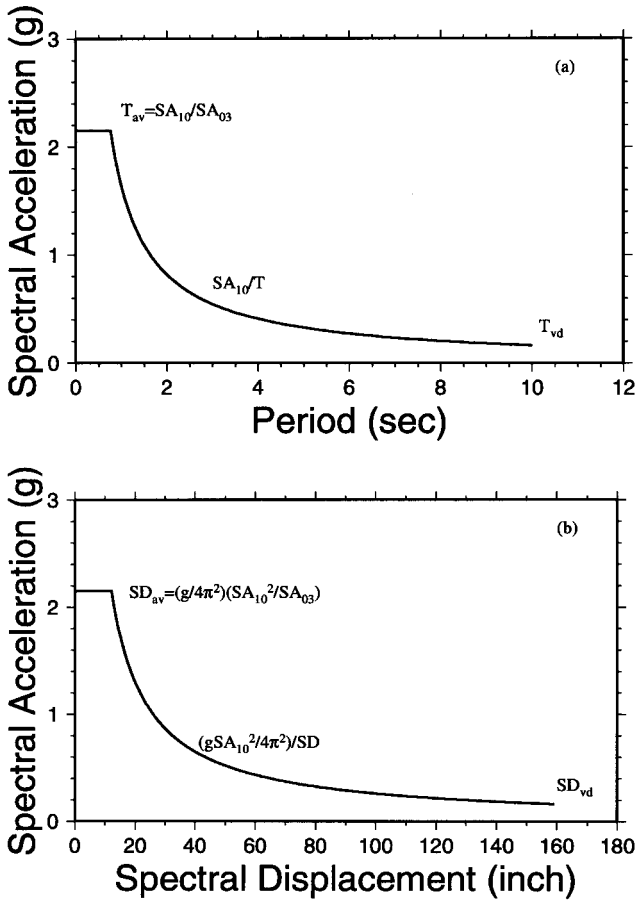

Figure A1. A sample of the elastic response spectrum as a function of period (a) and a function of SD (b).

$$\mathrm{SD} = \left(\frac{g}{4\pi^2}\right) T^2 \,\mathrm{SA}, \tag{A2}$$

and

$$T = 2\pi \left(\frac{\mathrm{SD}}{g\mathrm{SA}}\right)^{1/2}. \tag{A3}$$

In (A2) and (A3) g is the acceleration of gravity that is introduced because SA is measured in units of g. Substituting T in (A1b) by (A3) yields

$$\mathrm{SA} = \left(\frac{g\mathrm{SA}_{10}^2}{4\pi^2}\right)/\mathrm{SD}, \quad \mathrm{SD}_{\mathrm{av}} \le \mathrm{SD} \le \mathrm{SD}_{\mathrm{vd}}. \tag{A4}$$

We see that SA is proportional to 1/SD. Using (A1a) and (A4) we can convert Figure A1a into Figure A1b. The connecting point at T_{av} (Fig. A1a) is now at $\mathrm{SD}_{\mathrm{av}}$ (Fig. A1b). From $\mathrm{SA} = \mathrm{SA}_{03}$ and (A4), we have $\mathrm{SA}_{03} = (g\mathrm{SA}_{10}^2/(4\pi^2))/\mathrm{SD}_{\mathrm{av}}$ or $\mathrm{SD}_{\mathrm{av}} = g\mathrm{SA}_{10}^2/(4\pi^2\mathrm{SA}_{03})$. The connecting point at T_{vd} (Fig. A1a) is now at $\mathrm{SD}_{\mathrm{vd}}$ (Fig. A1b). From (A4) and (A1c), we have $\mathrm{SA}_{10}/\mathrm{T}_{\mathrm{vd}} = (g\mathrm{SA}_{10}^2/(4\pi^2))/\mathrm{SD}_{\mathrm{vd}}$ or $\mathrm{SD}_{\mathrm{vd}} = (g\mathrm{SA}_{10}/(4\pi^2))T_{\mathrm{vd}}$. Solving equations (A1c) and (A3), we have $\mathrm{SA} = (g\mathrm{SA}_{10}T_{\mathrm{vd}}/\mathrm{SD})^{1/2}/2\pi$ for the constant SD region.

Building Capacity Curve

Building capacity curve describes the building's lateral resistance to the lateral displacement (Manual, page 5-25). A building capacity curve has to be constructed for each building type. The key points on the curve are the yield point and the ultimate point (Fig. A2; Manual, page 5-26). It is assumed that up to yield point, the capacity curve is linear and then transits from elastic to nonlinear plastic states. The details of the nonlinear part are not provided in the Manual. We use part of an ellipse, which is less than a quarter of the ellipse (Fig. A2) to follow the nonlinear state (J. Bouabid, PBS & J, personal comm., 2002).

Two pairs of coordinates, (D_y, A_y) and (D_u, A_u), for the yield and ultimate points are passed by the capacity curve (Fig. A2). The following equation for an ellipse is used to get the nonlinear part of the curve:

$$\left(\frac{\mathrm{SD} - D_u}{C}\right)^2 + \left(\frac{\mathrm{SA} - A_x}{B}\right)^2 = 1. \tag{A5}$$

It is an ellipse centered at (D_u, A_x) with three parameters A_x, C, and B to be determined. We already have two equations to constrain the parameters because the curve has to pass the yield and ultimate points. We need one more equation and it comes from the yield point. To have a smooth connection between linear and nonlinear parts of the curve at the yield point, the slope of the tangent of the ellipse at the yield point should be the same as the slope of the linear part of the curve. From the derivative of an implicit function of (A5), we have

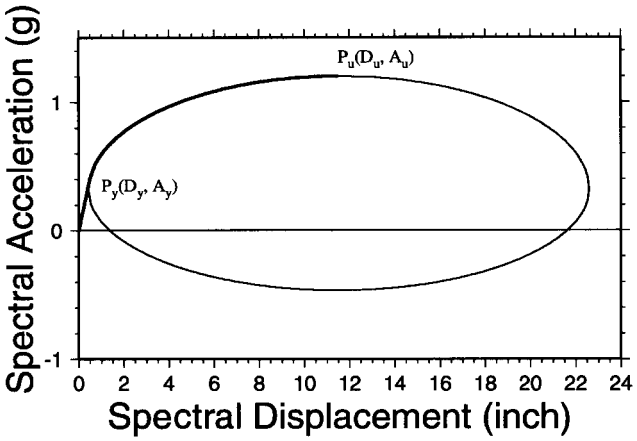

Figure A2. A sample of the building capacity curve. The thick line from the origin to the ultimate point P_u passing yield point P_y is the capacity curve. The ellipse shows how the capacity curve is constructed. The capacity curve has two parts: (1) from origin to the yield point is a straight line and (2) from the yield point to the ultimate point is overlapped with the ellipse. The straight-line part of the capacity curve is tangential to the ellipse at yield point.

$$d\mathrm{SA}/d\mathrm{SD} = -\left(\frac{\mathrm{SD} - D_u}{\mathrm{SA} - A_x}\right)\left(\frac{B^2}{C^2}\right), \tag{A6}$$

which should equal A_y/D_y when SD and SA take values of D_y and A_y, respectively. The coordinates for yield and ultimate points are given by HAZUS for each building type at different seismic design levels (Manual, pages 5-31 to 5-34). With the three relations discussed previously all three parameters, A_x, C, and B, can be determined.

Demand Spectrum and Damping Reduction

In HAZUS the demand spectrum is obtained by using the Newmark and Hall (1982) spectrum reduction factors to reduce the elastic spectrum discussed previously. The displacement at the cross point between the demand spectrum and the capacity curve is the SD for loss calculation. According to Newmark and Hall (1982, page 29), the response spectrum is defined as the maximum response of a single-degree-of-freedom system with damping to dynamic motion or force. It is important to recognize that damping levels depend on the level of deformation or strain in a structure.

The spectrum reduction factors R_a, R_v, and R_d for the constant SA, SV, and SD regions, respectively (Fig. A3), are given by Newmark and Hall (1982; referred to by Manual on page 5-64) as functions of the effective damping of a building, β_{eff}, as following:

$$R_a = 2.12/(3.21 - 0.68 \ln(\beta_{\mathrm{eff}})) \tag{A7}$$

$$R_v = 1.65/(2.31 - 0.41 \ln(\beta_{\mathrm{eff}})) \tag{A8}$$

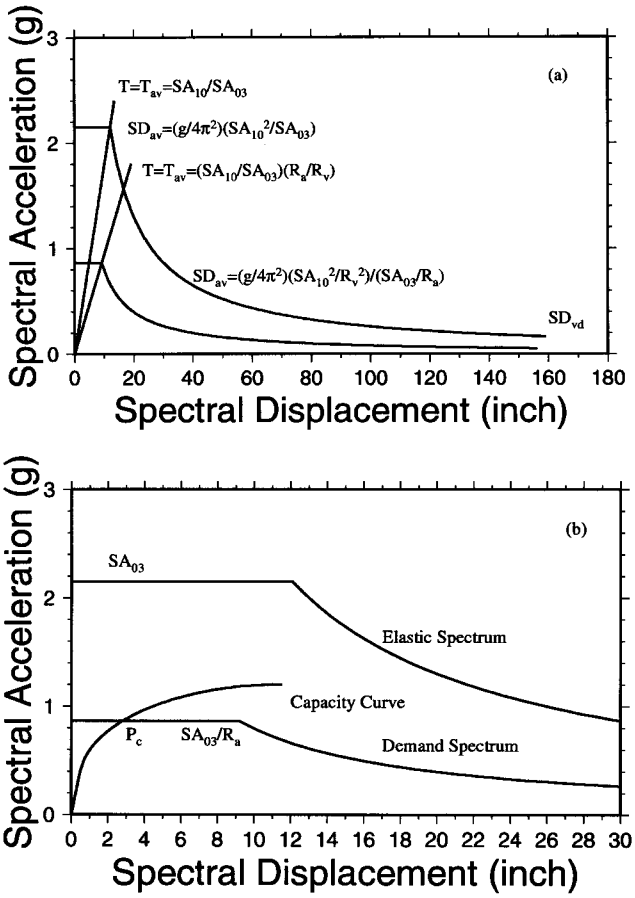

Figure A3. A sample of the demand spectrum and the intersection with the capacity curve. Panel (b) is similar to the schematic figure 5.7 of the Manual on page 5-67, except it is from real calculations. Any straight line from the origin represents a constant period in (a) when SA is expressed as a function of SD. Here, (b) is the same as (a) except only up to 30 inches displacement is plotted and the capacity curve is added to show the intersection with the demand spectrum.

$$R_d = 1.39/(1.82 - 0.27 \ln(\beta_{\text{eff}})). \quad \text{(A9)}$$

The effective damping β_{eff} is the sum of elastic damping β_e and hysteretic damping β_h (Manual, page 5-64):

$$\beta_{\text{eff}} = \beta_e + \beta_h.$$

The elastic damping β_e is not necessarily 5%. It depends on the building type. For example, it is 15% for light wood-frame buildings (W1 in HAZUS). The hysteretic damping depends on the area enclosed by the hysteresis loop at peak-response displacement D and acceleration A (Manual, page 5-65) as:

$$\beta_h = \kappa\left(\frac{\text{area}}{2\pi DA}\right),$$

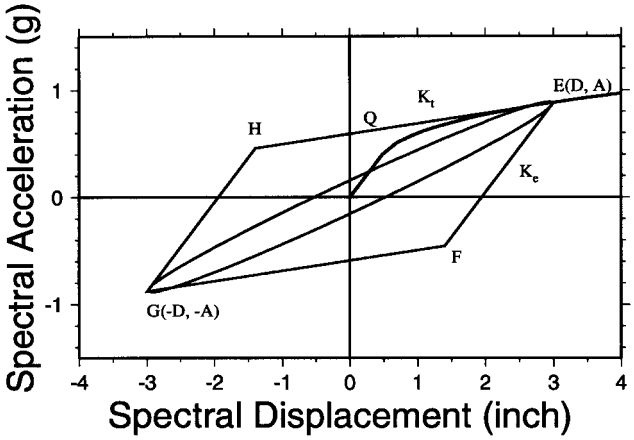

Figure A4. A schematic diagram to show the bilinear hystersis loop and the actual hysteresis loop. The bilinear loop is shown by the parallelogram *EFGH*. The ellipse in the parallelogram shows the actual loop. On the capacity curve, which starts from the origin, the point $E(D,A)$ is the intersection point with the demand spectrum (not shown). Line *EH* is tangential to the capacity curve at point $E(D, A)$ and has slope K_t; line *EF* is parallel to the linear part of the capacity curve and has slope K_e. The ellipse passes points $E(D,A)$ and $G(-D,-A)$. The area it covers is drawn arbitrarily. The ratio between the area sizes of the ellipse and the parallelogram is defined as κ.

where κ is a degradation factor. It is a function of shaking duration (Manual, page 5-66). The shaking duration (short, moderate, and long) is defined in HAZUS by earthquake magnitude (Manual, pages 5-65 and 5-66).

The area is the area enclosed by the hysteresis loop (Fig. A4), which is defined by a symmetrical push-pull of the building capacity curve up to peak positive and negative displacement D (Manual, page 5-64) at points $E(D, A)$ and $G(-D,-A)$. The HAZUS Manual does not provide a formula for the calculation of this area. We tested two versions of approximate formulas for calculating the area of a bilinear loop given in FEMA 274 (page 9-36, formula C9-50). Then we developed another formula that produces results much closer to the HAZUS software. The following is how the area is defined in our formulation (Fig. A4).

In Figure A4, the two sides *EF* and *EH* of the parallelogram *EFGH* have slopes of K_e and K_t. Here, K_e is the slope of the linear part of the capacity curve and $K_e = A_y/D_y$; the slope K_t is defined so that line *EH* is tangent to the capacity curve at point $E(D, A)$. So using (A6), we have

$$K_t = \left(\frac{D_u - D}{A - A_x}\right)\left(\frac{B^2}{C^2}\right).$$

Then we can derive an exact expression for the area of the parallelogram as

$$\text{Area} = 4(A - DK_e)(DK_t - A)/(K_e - K_t). \quad \text{(A10)}$$

The parallelogram in Figure A4 is a bilinear loop. The ellipse in the middle of the parallelogram represents the actual loop. The degradation factor κ is introduced to estimate the actual loop area from the bilinear hysteresis loop.

With the effective damping β_{eff}, we can calculate the reduction factors R_a, R_v, and R_d according to formulas (A7), (A8), (A9). The demand spectrum can be expressed using the reduction factors as:

$$\text{SA} = \text{SA}_{03}/R_a, \quad 0 \le T \le T_{\text{av}} \tag{A11}$$

and

$$\text{SA} = (\text{SA}_{10}/T)/R_{\text{v}}. \quad T_{\text{av}} \le T \le T_{\text{vd}}. \tag{A12}$$

Here we have followed the Manual (page 5-66) to ignore the details at short period and simply extend the constant SA region to period zero.

The period T_{av} now changes to a new value for the demand spectrum (Fig. A3a). According to equations (A11) and (A12), we have:

$$\text{SA}_{03}/R_a = (\text{SA}_{10}/T_{\text{av}})/R_v$$

or

$$T_{\text{av}} = \left(\frac{\text{SA}_{10}}{\text{SA}_{03}}\right)\left(\frac{R_a}{R_v}\right). \tag{A13}$$

It reduces to the original value of $\text{SA}_{10}/\text{SA}_{03}$ at 5% damping because $R_a = R_v = 1$ at 5% damping. According to the Manual (page 5-66), T_{vd} depends on the magnitude M not the effective damping. But according to Chopra (1995), T_{vd} will change from its original value (for example, 10 sec for M 7) for the elastic response spectrum to a new value for the demand spectrum (Chopra, 1995, page 221, figure 6.9.3). Note that formula (5-11c) of HAZUS, which is for the reduction of the constant SD region of a response spectrum (Manual, page 5-66), does not use R_d given by Newmark and Hall (1982), but uses a form like R_v. This treatment makes the connection at $T = T_{\text{vd}}$ smoother.

Using equation (A3), we can convert equation (A12) from a function of T to a function of SD similar to (A4) (Fig. A1):

$$\text{SA} = \left(\frac{g\text{SA}_{10}^2}{4\pi^2 R_v^2}\right)/\text{SD}. \quad \text{SD}_{\text{av}} \le \text{SD} \le \text{SD}_{\text{vd}}. \tag{A14}$$

Solving equations (A11) and (A14), we obtain the value for SD_{av} as:

$$\text{SA}_{03}/R_a = \left(g\text{SA}_{10}^2/(4\pi^2 R_v^2)\right)/\text{SD}_{\text{av}}$$

or

$$\text{SD}_{\text{av}} = g(\text{SA}_{10}^2/R_v^2)/(4\pi^2 \text{SA}_{03}/R_a).$$

These formulas are similar to the expressions for the elastic response spectrum (Fig. A1b), except that SA_{10} and SA_{03} are now reduced by the factors R_v and R_d, respectively.

When damping increases from 5%, R_a increases faster than R_v, so the factor (R_a/R_v) in (A13) is always larger than one and increases with damping. Therefore, the period of the connecting point between constant SA and constant SV of the demand spectrum is larger than the period of the same connecting point for the elastic spectrum (5% damping, Fig. A3a).

Peak-Response Displacement and Acceleration

In the preceding sections, we have summarized how to build a building capacity curve from given coordinates of the yield and ultimate points and an elastic response spectrum from given ground-motion parameters SA_{03} and SA_{10}. If the final peak-response displacement and peak-response acceleration are known, we are able to calculate the effective damping and the reduction factors to get the demand-response spectrum from the 5% damped elastic response spectrum. A simple iterative process is needed to find the final peak-response displacement and acceleration. Because the response spectrum and the capacity curve are monotonically decreasing and increasing functions of SD, respectively, the convergence of iteration is guaranteed. The crossing point P_c between the capacity curve and the demand spectrum in Figure A3b shows the solution of the iteration. Once the peak-response displacement and acceleration are solved, the next step is to build the fragility curves, which will return the damage probabilities for different damage states for given SD.

Building Fragility Curves

Building fragility curves are the lognormal probability functions for the structural and nonstructural damage states to be reached or exceeded when the peak-response displacement D is given (Manual, page 5-4). The building damage states are classified into five discrete levels: none, slight, moderate, extensive, and complete. These damage states are directly related to the percentage of building-replacement cost. A fragility curve for a particular damage state $ds(i)$ ($i = 0, 1, 2, 3,$ and 4 for these five damage states) is defined by a median value m_i of the peak-response displacement and by the variability β_i which is associated with the damage state:

$$P(\text{DS} \ge ds(i) | \text{SD} = D) = \frac{1}{\beta_i (2\pi)^{1/2}} \int_0^D \frac{1}{S_d} \exp\left\{ - \frac{(\ln(S_d/m_i))^2}{2\beta_i^2} \right\} dS_d, \quad i = 1, 2, 3, 4. \tag{A15}$$

This formula is written according to our understanding of

formula (5-2) in the HAZUS manual (page 5-5). It is a cumulative probability density function. For $i = 0$, the preceding probability is always one. The values of β_i and m_i can be found in table 5.9a of the Manual (page 5-41) for different types of buildings. The preceding expression can be rewritten in a more compact form by using the error function *erf*:

$$P(\mathrm{DS} \le ds(i) | \mathrm{SD} = D) = \frac{1}{2}\left(1 + erf\left(\frac{\ln(D/m_i)}{\sqrt{2}\beta_i}\right)\right), \quad i = 1, 2, 3, 4. \quad \text{(A16)}$$

A sample plot for the four fragility curves can be found in the Manual on page 5-4.

The probability density functions $p_i(D)$ ($i = 0, 1, 2, 3, 4$) for each damage state can be derived from the preceding cumulative probability density functions as:

$$p_i(D) = P(\mathrm{DS} \ge ds(i) \mid \mathrm{SD} = D) - P(\mathrm{DS} \ge ds(i+1) \mid \mathrm{SD} = D), \quad i = 0, 1, 2, 3$$

and

$$p_4(D) = P(\mathrm{DS} \ge ds(4) \mid \mathrm{SD} = D). \quad \text{(A17)}$$

Figure A5 shows these five density functions from a real calculation.

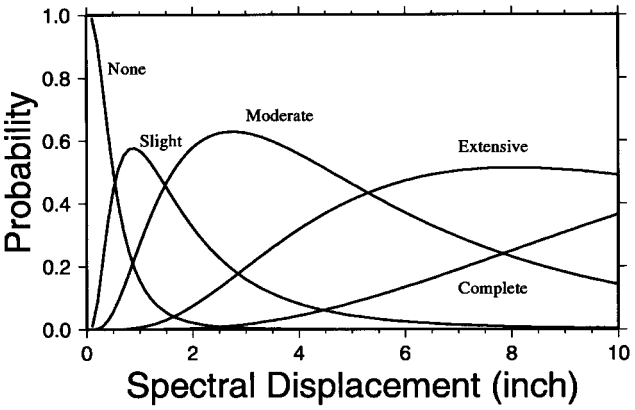

Figure A5. Five damage probability functions. These curves are calculated according to formula (A17).

Estimation of Loss Ratio

The loss ratio to the building structure or nonstructural systems can be calculated as the following summation of the loss ratios for the damage states multiplied by the probability densities for those damage states:

$$\mathrm{Loss}(\%) = \sum_{i=1}^{4} p_i(D) R_i, \quad \text{(A18)}$$

where R_i is the direct economic loss as a percentage of the replacement cost for damage state $ds(i)$. The replacement cost is not defined as the replacement cost of the whole building but only the part related to a particular type of damage. For example, if the structural damage is considered, the replacement cost is for replacing the structure not the whole building. We call R_i the damage rate for damage state $ds(i)$. If we want to calculate the loss rate for the wood-frame residential buildings, for example, we will apply equation (A18) four times for the structural, nonstructural drift-sensitive, nonstructural acceleration-sensitive, and content losses. The damage probability P_i does not change for the same damage state, but R_i changes between different types of damages. Thus, we can calculate four loss ratios for the four damage types.

California Geological Survey
801 K Street, MS 12-32
Sacramento, California
(T.C.)

U.S. Geological Survey
Box 25046 Federal Center, MS 966
Denver, Colorado 80225
(M.D.P.)

Manuscript received 23 June 2005.